2024 IEEE/ASME International Conference on Advanced Intelligent Mechatronics (AIM)
July 15-19, 2024. Boston, MA, USA

Computer-Vision-Based Autonomous Robotic Part Repairing*

Baihui Chen[1], Liwen Hu[1], ElHussein Shata[1], Shashank Shehkar[2], Charif Mahmoudi[2], Yuebin Guo[1], Qingze Zou[†,1]

***Abstract*— In this paper, a computer-vision(CV)-based robotic autonomous part repairing system is developed. Robotic autonomous part repair is needed to retrofit high-value parts as robotic-based machining system offers advantages in manufacturing flexibility, adaptability, precision, and low cost. Although CV-based robotic manipulation has been explored for applications, challenges emerge in CV-based robotic machining applications due to the more stringent precision and accuracy in part identification, the inevitable eccentric misalignment in data acquisition, the artifacts of the laser-scanned data, and the needs for simultaneous force and path tracking. The contribution of this work is the development of an experimental-based approach to quantify and compensate for the eccentric misalignment, and then, identify and quantify the defect on the part. We illustrate the function and performance of the CV-based robotic autonomous repairing through experiment.**

I. INTRODUCTION

In this paper, a computer-vision(CV) based robotic autonomous part repairing system is developed. Robotic autonomous repairing is needed to retrofit defected, worn parts of high value, such as jet engine blades [1] and tank drive shaft. Along with the evolution of advanced manufacturing, we also witness that human skills needed for repairing these high-value parts become increasingly scarce. Compared to complicated CNC machines, robotic autonomous part repairing offers the advantages in manufacturing flexibility, adaptability, precision, efficiency, and relatively low cost [2]. However, existing work on CV-based robotic manipulation are not directly applicable due to the challenges to meet the high precision needed in manufacturing machining [2].

Limitations exist in current work in CV-based robotic manipulation for machining operations including the part repairing [3]. Computer-vision has been utilized in robotic application in manufacturing for subject grabbing and translation [4], where the images acquired have been used to identify, and locate the subject [5] and predict its trajectory (for moving subject) [6]. The spatial resolution of the position and trajectory quantified, however, is not as precise as that needed in machining operations. CV-technique has also been developed for human-robot-interaction applications [7], where the images acquired have been utilized to estimate and predict human's motion/behavior. Although more complicated image information needs to be processed, the accuracy and precision of the position identification are not as demanding as in machining operation either. In these two major applications of CV-based robot manipulation, the research focus is on the recognition and identification of the subject in more complicated environment/situation and hand-eye calibrations [8]. Whereas in robotic-based for machining, the goal is to accurately identify the defect and precisely repair the defects (either by subtraction or addition of materials) at high efficiency. Thus, techniques need to be developed for CV-based robotic autonomous machining.

Challenges exist in achieving high-precision machining in robotic-based part repairing. Given the sub-millimeter precision needed in machining operation, laser-scanning-based visual sensing is preferred over RGB-D sensor and stereo-camera [9], and fix mounting (of the laser scanner) is preferred over direct mounting (on the robot end effector) [10]. However, as the part usually is mounted to a rotary stage for machining (as schematically shown in Fig. 1), extraneous error can be induced to the scanned data—due to the misalignment of the rotation axis with respect to the geometric center line of the part, resulting in additional fluctuations to the scanned data. Such an eccentric rotation misalignment, however, tends to be not directly measurable. Additional fluctuation to the scanned data can also be induced by the inevitable misalignment (albeit small) of the laser scanning to the axial direction of the part. Challenges can also arise from the artifacts induced by the rapid and "spikes" like topography features of the part, and accurate identification of the defect.

In this paper, a CV-based robotic part repairing system is developed. A fix-mounted laser scanner is used to capture the 3D topography. Specifically, an experiment-based approach is proposed to quantify the eccentric misalignment in the scanned data by scanning of a standard part. The standard part is also used to quantify the scanner-tilt error and for calibration. The defect is identified from the scanned 3D topography data by comparing to the defect-free part. Experimental results show that accurate milling in defect repairing is achieved.

II. ROBOTIC PART DEFLECT REPAIRING

A. System Description

The overall robotic repairing system is schematically shown in Fig. 1, where a robot equipped with a machining end effector (e.g., milling) is used to repair the defects on

*The authors would like to thank the financial support from the DOE/CESMII (grant # DE-EE0007613), and the Siemens Corporation, Technology (grant # 830392).

†Corresponding author. (e-mail: qzzou@soe.rutgers.edu)

1The authors are with the Department of Mechanical and Aerospace Engineering, Rutgers University, Piscataway, NJ, 08854, USA.

2The authors are with the Siemens Corporation Technology, Princeton, NJ 08540, USA.

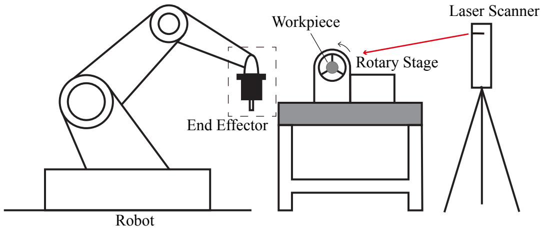

Fig. 1. Computer-vision-based robotic part defect repairing system.

the workpiece clamped to a rotary stage mounted on a work station table. A profile laser scanner is placed at a fixed location to capture the topography of the workpiece when it is rotated by the stage.

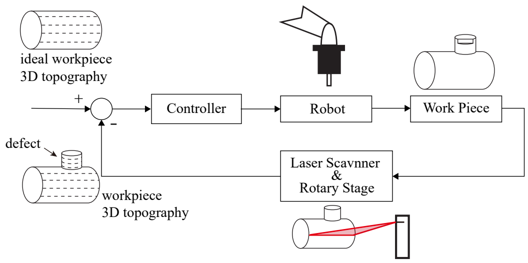

Fig. 2. Workflow of the CV-based autonomous part defect repairing.

As shown in Fig. 2, the repairing starts with capturing the 3D topography of the workpiece, then comparing the topography to that of the defect-free reference workpiece to identify the defect, which, in turn, is used to plan the machining path and motion of the robot, and the defect is repaired in a line by line, and layer by layer manner. This scanning, identification and repair process is repeated until the entire defect is finished.

B. Problem Statement

Errors and uncertainties must be addressed in the above CV based robotic part repair process. First, errors can be induced to the scanned topography by the misalignment between the rotation axis and the geometric center axis of the stage chuck, due to the inevitable error (albeit small) in the stage installation. As a result, extraneous fluctuation is introduced to the topography data obtained. For example, when a cylinder workpiece is scanned in the longitudinal rotation x-axis direction (i.e., with the laser beam parallel to the x-axis, see Fig. 3 (a1), the scanned line-by-line data from a complete round of rotation would form a flat surface parallel to the x-t plan if there were no eccentric misalignment (see Fig. 3 (a2), where the z axis is pointing to the laser scanner). However, a wavy surface is generated (see Fig.3 (b2)). The topography variation induced will directly lead to errors of identified coordinates of defects.

Additional issues exist in autonomously identifying the defect from the laser scan data. First, acute geometric change in the part shape may result in false identification, (e.g., small cavities mistakenly identified as tiny bumps), which interferes with the scanning result. Moreover, the defect on a part cannot be directly identified from the scanned 3D-point cloud obtained, as the reference point

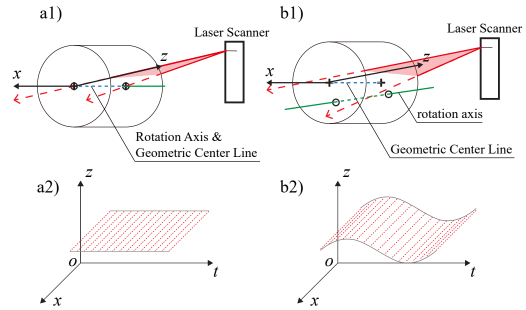

Fig. 3. Comparison of (a1) the scanning of a cylinder without to (b1) that with the rotation-geometry axis misalignment; (a2), (b2) the corresponding scanned data obtained after one complete rotation, respectively.

cloud are not in the same frame of the scanned one. Finally, to design and plan the robot path, the frame transformation from the laser scanner to the robot end effector must be accurately calibrated. Thus, in this work we aim to address these issues by achieving the following objectives:

- $\mathbb{O}$.1 Quantify and compensate for the eccentric-misalignment of the rotary stage;
- $\mathbb{O}$.2 Quantify and eliminate the 3D rebuild error caused by laser scanner offset;
- $\mathbb{O}$.3 Identify the location of the defect with respect to the defect-free reference;
- $\mathbb{O}$.4 Calibrate the transformation matrix between the laser scanner and the robot end effector (i.e., called *eye-to-hand calibration* below), and plan the operation path of the end effector.

III. Computer-vision-based Robotic Part Defect Repairing

A. Eccentric Rotation Misalignment Quantification

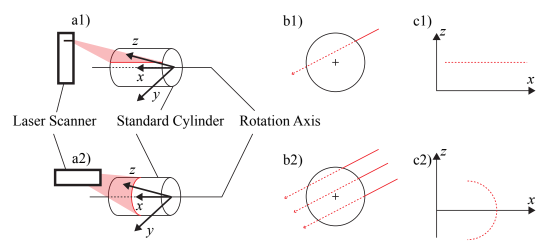

Fig. 4. (a1) Laser scanning in the lateral direction, (b1) the corresponding side view, (c2) the data obtained in one-scan presented in the x-y axis plane, and (a2, b2, c2) the counter part of (a1) to (c1) for scanning in the vertical direction, respectively.

The challenge in quantifying the eccentric misalignment (called the *center-to-rotation misalignment* below) is that it is very difficult (if not impossible) to measure the center line and the rotation axis directly. We propose to identify the eccentric misalignment error by scanning a cylinder part of well-defined dimension and surface quality. Particularly, when scanning the cylinder part in the vertical direction as in Fig. 4 (a2), the laser scan data obtained at any given rotation angle would form a circle, if there were no eccentric alignment and the scanning is exactly in the vertical direction, as shown in Fig. 4 (b2, c2). Thus, the deviation of the scanned data from this ideal circle can be utilized to quantify the center-to-rotation misalignment.

Specifically, the distance and the angle between the rotation axis of the chuck and the center axis of the cylinder, d_{rc} and α_{rc}, called the *center-to-rotation distance and angle* below, respectively (see Fig. 5), will be quantified by using the scan data collected from one complete revolution of the cylinder.

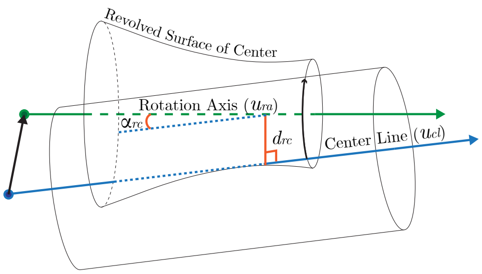

Fig. 5. The revolved hyperbolic surface formed by the center line of the standard cylinder rotates around the rotation axis for one revolution.

Our approach is based on the fundamental relation of any two arbitrary lines in 3D-space: the angle α_{rc} and the distance d_{rc} between the rotation axis and center line is by

$$\cos\alpha_{rc} = \vec{u}_{cl} \cdot \vec{u}_{ra},\ d_{rc} = |(\vec{u}_{cl} \times \vec{u}_{ra}) \cdot \vec{v}_{OC}|, \quad (1)$$

where $\vec{u}_{ra}$ and $\vec{u}_{cl}$ are the unit vectors of the rotation axis and the cylinder center line, and $\vec{v}_{OC}$ is a vector from any given point C on the center line to any given point O on the rotation axis (see Fig. 5). Thus, the problem is converted to quantifying the vectors $\vec{u}_{ra}$, $\vec{u}_{cl}$, $\vec{v}_{OC}$ from the scanned data. In the presence of the center-to-rotation misalignment, after the stander cylinder rotates a complete round w.r.t. the rotation axis, the center line of the cylinder would form a one sheet hyperbolic surface (see Fig. 5). As in practice the laser beam scan is not perfectly aligned with the vertical direction as in Fig. 4 (a2-c2), the intersection of the laser scanning plan (on which the laser beam is) across this hyperboloid curve will form an ellipse instead of a circle (called the ellipse $\mathcal{E}_i$ below), as shown in Fig.6. Both the hyperboloid curve and the ellipse $\mathcal{E}_i$ can be obtained from the scanned data (described in Sec. 3.2 later), thus the problem now is converted to quantifying the vectors $\vec{u}_{ra}$, $\vec{u}_{cl}$ and $\vec{v}_{OA}$ by using the hyperboloid curve and the ellipse $\mathcal{E}_i$.

Specifically, we consider the two center lines that crosses the laser plane where the corresponding intersection points forms the major axis of the ellipse $\mathcal{E}_i$. As shown in Fig. 6, these two intersection points are denoted as Point A and Point B, respectively, and the two center lines are called Center-line A and Center-line B, respectively. To identify the vector $\vec{u}_{cl}$, we consider the counterpart of point A and point B on the center line-B and the center line-A, point A' and point B', respectively, as shown in Fig. 6, i.e., point $A'(B')$ is obtained when the center line-A(center-line B) rotates (around the rotation axis) and overlaps with the center line-B(center-line A). The corresponding rotation angle ϕ (see Fig. 6) can be quantified directly from the scanned data (described in Sec.3.2 below), and finding the unit vector $\vec{u}_{cl}$ is equivalent to finding the vector $\vec{v}_{AB'}$ or $\vec{A'B}$, as

$$\vec{u}_{cl} = \frac{\vec{v}_{AB'}}{|\vec{v}_{AB'}|}. \quad (2)$$

Thus, we show that $\vec{u}_{ra}$ an $\vec{v}_{AB'}$ can be obtained from the length of line segment AB, ℓ_{AB}; the angle between the center line-A and the laser plane, $\beta_{AB'}$; the angel between center line-B and the laser plane, $\beta_{A'B}$ and the rotation angle, ψ.

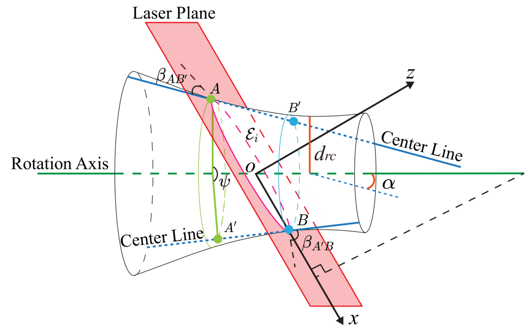

Fig. 6. The geometric relation between the laser plan and the one sheet hyperbolic surface is formed by the center line's rotating around the rotation axis, and the center-to-rotation distance and angle, d_{rc} and α_{rc}.

We start with specifying the coordinate used: Let the line of the major axis AB be the x-axis, the laser plane be the xy-plane, and the intersection of the rotation axis and the laser plan be the origin O (see Figs. 6 and 6). Then, the vector $\vec{v}_{OA} = [x_A, 0, 0]^T$, where x_A is the x-coordinate of point A, and, the vector $\vec{v}_{OB} = [x_B, 0, 0]^T = [x_A - \ell_{AB}, 0, 0]^T$. As the rotation axis is in the xz-plan, the unit vector of the rotation axis is given by

$$\vec{u}_{ra} = [x_{ra}, 0, \sqrt{1 - x_{ra}^2}]^T, \quad (3)$$

Thus, vector $\vec{v}_{OA'}$ and $\vec{v}_{OB'}$ can be represented in terms of vectors $\vec{v}_{OA}$ and $\vec{v}_{OB}$ as

$$\begin{aligned}\vec{v}_{OA'} =& \cos(\psi)\vec{v}_{OA} + (1 - \cos(\psi))(\vec{v}_{OA} \cdot \vec{v}_{ra})\vec{v}_{ra} \\ &+ \sin(\psi)\vec{v}_{ra} \times \vec{v}_{OA}, \quad (4)\\ \vec{v}_{OB'} =& \cos(-\psi)\vec{v}_{OB} + (1 - \cos(-\psi))(\vec{v}_{OB} \cdot \vec{v}_{ra})\vec{v}_{ra} \\ &+ \sin(-\psi)\vec{v}_{ra} \times \vec{v}_{OB}. \quad (5)\end{aligned}$$

Representing the above two vector equations in the coordinate of Figs. 6 leads to

$$\vec{v}_{OA'} = \begin{bmatrix} x_{A'} \\ y_{A'} \\ z_{A'} \end{bmatrix} = \begin{bmatrix} x_A(\cos(\psi)(1 - x_{ra}^2) + x_{ra}^2) \\ x_A \sin(-\psi)\sqrt{1 - x_{ra}^2} \\ (1 - \cos(\psi))\sqrt{1 - x_{ra}^2} \end{bmatrix}, \quad (6)$$

$$\vec{v}_{OB'} = \begin{bmatrix} x_{B'} \\ y_{B'} \\ z_{B'} \end{bmatrix} = \begin{bmatrix} (x_A - \ell_{AB})(\cos(\psi)(1 - l^2) + x_{ra}^2) \\ (x_A - \ell_{AB})\sin(\psi)\sqrt{1 - x_{ra}^2} \\ (1 - \cos(\psi))\sqrt{1 - x_{ra}^2} \end{bmatrix}. \quad (7)$$

Thus, $v\vec{_{AB'}}$ and $v\vec{_{A'B}}$ can be specified as

$$v\vec{_{AB'}} = [x_A - x_{B'}, -y_{B'}, -z_{B'}]^T, \quad (8)$$
$$v\vec{_{A'B}} = [x_{A'} - (x_A - \ell_{AB}), y_{A'}, z_{A'}]^T, \quad (9)$$

and the projection of $\vec{v}_{AB'}$ and $\vec{v}_{A'B}$ to the laser plan are

$$\cos(\beta_{AB'}) = \frac{\vec{v}_{AB'} \cdot \vec{u}_z}{|\vec{v}_{AB'}|},\ \cos(\beta_{A'B}) = \frac{\vec{v}_{A'B} \cdot \vec{u}_z}{|\vec{v}_{A'B}|}, \quad (10)$$

respectively, where $\vec{u}_z = [0, 0, 1]^T$ is the z-axis unit vector. As both the length of the segment AB, ℓ_{AB} and the angle

$\beta_{AB'}$ and the angle $\beta_{A'B}$ can all be quantified from the scanned data (explained immediately below in Subsec. 3.2), combining Eqs. (6-10) shows that the only two unknown parameters, x_A and x_{ra} in Eqs. (6, 7) , can be obtained by solving Eq. (10) after substituting Eqs. (6, 7) into Eqs. (8, 9) and then into Eq. (10). Angle α_{rc} and distance d_{rc} can be obtained via Eq. (1).

B. Variables Quantified from the Scanned Data

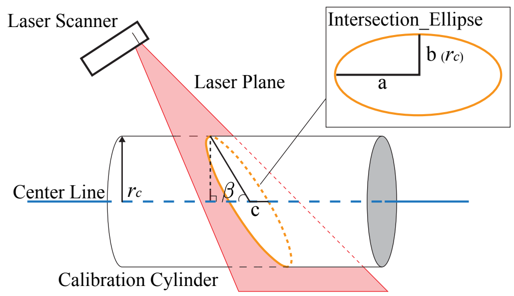

Fig. 7. The ellipse intersection between the laser beam and the calibration cylinder when the scanning is not exactly in the vertical z-axis.

Next we discuss how to quantify, from the scanned data, the length of the major axis of the ellipse $\mathcal{E}_i$, ℓ_{AB}, the angle between the laser plane and the center line, $\beta_{AB'}$ and $\beta_{A'B}$, and the rotate angle from center line-A to center line-B, ψ. First, at any rotation angle ω, the reflected laser beam obtained from the vertical scanning configuration forms an ellipse, called the surface-intersection ellipse $\mathcal{E}_s$ (θ) below, if the scanning is not precisely aligned (see Fig. 7). The ellipse $\mathcal{E}_i$ is collectively formed by the intersections of the center of this ellipse $\mathcal{E}_s$ (θ) with the center line obtained at each sampled rotation angle ω (point c in Fig. 7). Thus, the ellipse $\mathcal{E}_i$ can be obtained from the scanned data by fitting the laser beam scanned data at every sampled rotation angle to an ellipse, finding the center of that ellipse (i.e., point c), and then, fitting all the center points into an ellipse. As a result, the length of major axis ℓ_{AB} is obtained.

Considering the case where the cross section point coincides with the point A, $\beta_{AB'}$ is formed by the projection of the center line AB' to the laser plan, and the projected line overlaps the major axis of $\mathcal{E}_s$. The angle between the center line and the laser plane is $\beta_{AB'}$ is $\beta_{AB'} = \frac{\pi}{2} - \cos^{-1}\left(\frac{a_{AB'}}{r_c}\right)$, where $a_{AB'}$ equals to the half of the major axis of ellipse E_s, obtained from the fitted surface-intersection ellipse $\mathcal{E}_i$ $(\beta_{AB'})$, and r_c equals to the radius of the standard cylinder. Finally, ψ can be obtained by the rotation time t_{AB} (time to rotate from point A to point B in Fig. 6), and ω as $\psi(t_{AB}) = \omega t_{AB}$.

Thus, the above quantified eccentric alignment, α_{ra} and d_{ra}, can be used to correct the scanned result. Particularly, during the defect repairing machining, the part will be scanned in the horizontal direction shown in Fig. 4 (a1), where the x-axis is the longitudinal horizontal direction, z-axis is parallel to the laser plane, and the origin is chosen as the first scanned location of interests on the part. This calibration process amounts to translating the above horizontal scanning coordinate to the inner coordinate of the laser scanner itself, and accounting for the inevitable misalignment of the scanner. The quantified eccentric misalignment is used in the calibration and identification of the coordinate translation.

C. 3D Point Cloud Construction

The defect is identified by comparing the topology data of the part to that of the defect-free part or via laser scan. The scanned data $\vec{v}^{\ell}(t) = [x_\ell(t), z_\ell(t)]^T$, can be transformed from the laser scanner frame to the table frame to the milling frame as

$$\vec{v}^m = R_\ell^m [x_\ell(t), 0, z_\ell(t)]^T + P_\ell^m, \tag{11}$$

with $R_\ell^m = R_T^m(\theta(t))R_\ell^T$, $P_L^m = R_\ell^m P_\ell^T$, where $x_\ell(t)$ and $z_\ell(t)$ are the scanned x- and z- axis data in the laser frame, R_L^T and $R_T^m(\theta(t))$ are the rotation matrix from the laser frame to the table frame and from the table frame to the milling frame, respectively, with $\theta(t) = \omega t$, P_L^T is the translation vector from the laser frame to the table frame. The rotation matrix R_L^T can be calibrated by the scan data of standard cylinder in the lateral direction.

The 3D point cloud of the CAD model will be interpolated to be aligned to the scanned data. The sampled point on the scanned 3D point cloud $\vec{v}^R$ is mapped to corresponding position on interpolated CAD model, $\vec{v}^{CAD}$ is given by $\vec{v}^{CAD} = R_m^{CAD}\vec{v}^m + P_m^{CAD}$, where R_m^{CAD}, P_R^{CAD} are obtained using iterative closest point (ICP) algorithm [11].

Then, the defect can be identified by using the 3D point cloud data and the above transformed CAD mode using the ICP algorithm. The defect 3D-point cloud is then used to design the path for repairing. Particularly, we plan the path by choosing the starting point at the furthest location on the defect (from the robot end effector), and plan the path along the longitudinal direction (x-axis of the table frame) of the defect.

IV. MILLING EXPERIMENT AND EXAMPLE

A. Experimental Setup

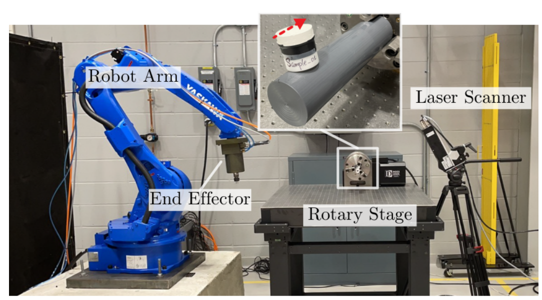

Fig. 8. The overview of the CV-based robotic part defect repairing system, where the inserted picture in the upper middle of the figure shows the added cylinder to mimic the defect.

The CV-based robotic repairing system developed is shown in Fig. 8. We started with quantifying the eccentric misalignment. A standard cylinder part was scanned to quantify the center-to-rotation angle and distance, α_{rc} and d_{rc}. To improve the accuracy of the misalignment quantification, the standard part was scanned at three different locations. The scanned data was used to construct the surface-intersection ellipse $\mathcal{E}_s(\theta)$ for each rotation angle, and then the center of each ellipse $c(\beta)$ was quantified and used to construct the ellipse, $\mathcal{E}_i$. Then α_{rc} and d_{rc}, were obtained. To evaluate the accuracy of eccentric misalignment, the scanned data standard cylinder part with or without accounting for the center-to-rotation angle and distance were compared to their normal values (provided by the manufacturer), respectively.

Next the defect was identified and quantified, and the repairing path was designed based on the experiment results. The defected part was scanned in the longitudinal lateral direction. The scanned 2D-data were converted to 3D-point cloud via Eq. (11). The 3D-point cloud of the defected part was compared to that of the defect-free reference via the sampling alignment and transformation based on the ICP algorithm. Then, the 3D point cloud of the defect part were used to design the repairing path. Specifically, a clay was attached to a plastic pipe, and 16 small markers were made via the robotic milling end effector (see Fig. 11 (a)).

The coordinates of the hole markers were measured using the laser scanner and then used to quantify the transformation frame accordingly. Finally, one milling path was designed to demonstrate the repairing operation. A straight line at the edge of the defect-cylinder in the longitudinal x-axis in the table frame was designed and followed by the milling end effector, with the feeding depth set at 5 mm, and the cut width selected as the radius of the milling cutter at 6.35, respectively. After the one-line milling operation, the machined defect part was scanned by the laser scanner to evaluate the repairing quality.

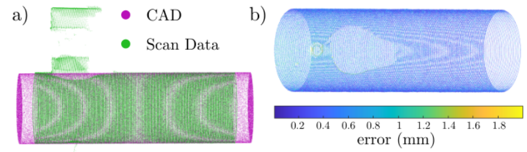

Fig. 10. (a) Comparison of the 3D-point cloud of the defected part to that of the defect-free reference, and (b) the 3D-point cloud of the difference.

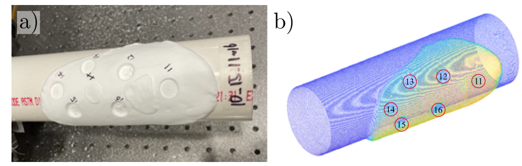

Fig. 11. (a) The 16 markers on the clay part for calibration, and (b) the corresponding 3D-point cloud scanned data obtained.

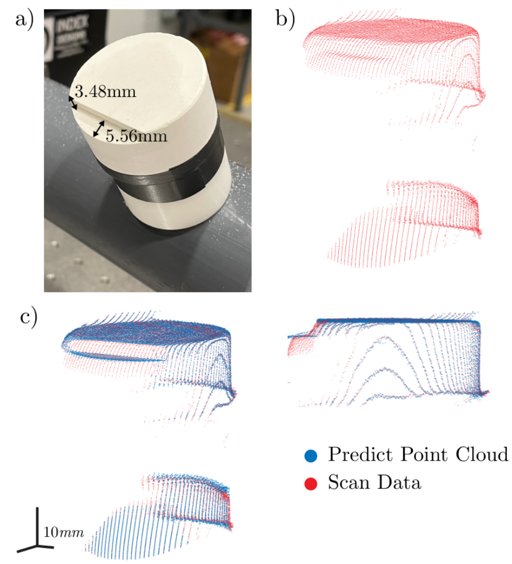

Fig. 12. (a) The defect portion after the one-cut milling, (b) the corresponding 3D-point cloud obtained from scanning after the milling, and (c) the comparison of the 3D-point cloud of the part after the one-line milling to that of the predicted one, where the point cloud on the right shows the zoomed-in view of the milling part.

B. Experimental Results and Discussion

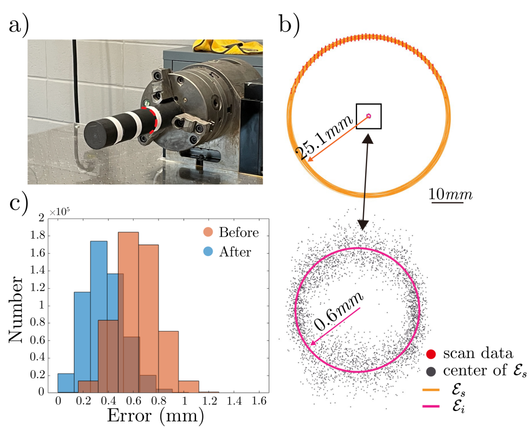

Fig. 9. (a) The three white ribbons that marked the vertical scanning location in the eccentric misalignment quantification, (b) the scanned data (red cross) and the fitted ellipses $\mathcal{E}_s(\theta)$ obtained from the three vertical scanning, and the centers of those fitted ellipses $\mathcal{E}_s(\theta)$ in (b) and the fitted ellipse (circle), respectively, and (c) The scan 3D point cloud of the standard cylinder before and after quantification.

The eccentric misalignment quantification results are shown in Fig. 9 (b) and (c). First, the scanned data obtained from the three vertical scanning were compared to each other—the scanned 2D $[z_v(t), x_v(t)]^T$ at the same rotation angle in each vertical scanning were compared to each other. The difference were less than 0.2 mm in both the z- and x- axis direction for all rotation angles, respectively, similar to the resolution of the laser scanner in the z- and x- axis around 0.2 mm and 1.0 mm, respectively. This implied that the rotation-to-center angle α_{rc} was small and close to zero, i.e., $\alpha_{rc} \approx 0$, and the scanning can be treated as exactly in the vertical direction, i.e., the projection angle of the center line to the laser beam plan $\beta \approx 90°$. As such, the cross-section ellipse $\mathcal{E}_s(\theta)$ became a circle for each rotation angle, and the center-to-rotation ellipse became a circle too. The measured vertical scanned data in all the three scanning are shown in Fig. 9 (b), along with the fitted circles, and the centers of these circles and the fitted ellipse (circle) of these centers are shown in the zoomed-in view. The difference of the scanned data for the standard cylinder part with and without accounting for the eccentric misalignment with respect to the nominal manufacturer values are compared in

Fig. 9 (c).

The 3D point cloud of the defected part obtained by using the obtained frame transformation R_m^{CAD} is compared to the defect-free reference obtained from a CAD model in Fig. 10 (b). The 3D point cloud of the 10 marks chosen to quantify the transformation matrix from the table frame to the robot base frame overlapped to the desired location, as shown in Fig. 11 (b). The one-line milling machine on the defect of the part is shown in Fig. 12 (a), and the 3D-point cloud of the part after this machining is shown in Fig. 12 (b). Finally, we compared the 3D-point cloud of the defect part after this one-line machining to the predicted one in Fig. 12 (c).

The experimental results showed that by using the proposed experimental-based approach, the eccentric misalignment were accurately quantified. The radius of all the fitted circles (ellipses), $\mathcal{E}_s$, from the three vertical scanning was at 25.1 ± 0.8 mm. The variation at 0.8 mm was within the precision level of the scanner. The circles (ellipses), $\mathcal{E}_i$, had a radius of 0.6 ± 0.08 mm, where the variation of 0.08 mm was below the resolution of the laser scanner. The accuracy of the identified center-to-rotation distance $d_{rc} = 0.6$ mm can also be seen from the difference of the scanned data to the ”true” value (the nominal value). As shown in Fig. 9 (c), the deviation from the ”true” value was substantially reduced, with the difference mostly occurred at 0.3 mm , reduced by over 50% from > 0.6 mm if not compensated for. Therefore, the experimental results demonstrated the efficacy of the proposed approach in accurately quantifying the eccentric misalignment error.

The experimental results also showed that the defect can be accurately identified and quantified by using the proposed technique. The accuracy of the 3D-point cloud construct directly affected the accuracy of the comparison of the 3D-point cloud of the defected part to that of the CAD model. As shown in Fig. 10 (b), the two 3D point cloud overlapped each other well in the common portion.As such, the defect can be accurately identified and quantified (see Fig. 10 (c)).

Finally, the preliminary milling repairing operation demonstrated that autonomous robotic repairing can be achieved in the system developed. As shown in Fig. 11 (b), the variations of the transformation matrix (from the table frame to the robot base frame) quantified by using the 10 markers was, small at 1.25 mm, close to the resolution of laser scanner x-axis at 1.0 mm. As shown in Fig. 12 (a), the geometric shape and surface quality of the one-line milling cut result were close to the desired visually. The width and depth of the cut at 5.56 mm and 3.48 mm were close to the designed value at 6.35 mm and 5 mm respectively. The precision of the milling machine result can also be seen from Fig. 12 (c): The 3D point cloud of the machined part and that of the predicted one were close to each other. Thus, this preliminary experimental implementation of the CV-based robotic machining system illustrated the effectiveness of this system in precision repairing machining.

V. Conclusion

A CV-based autonomous robotic repairing system has been developed in this work. A high-precision laser scanner placed at a fixed location was employed to identify and quantify the defects of a part mounted on a rotary stage, and guide the robot milling end effector for defect machining in real-time. An experiment-based approach was proposed to compensate for the effect of the eccentric rotation on the laser scanned data, caused by the misalignment of the rotation axis to the center line of the rotated part. The defect was identified through the comparison of the scanned data of the defected part to that of a defect-free reference, obtained from a CAD model. The hand-to-eye transformation was calibrated experimentally using the scanner. Experimental implementation in a milling operation mimicking part repairing was conducted and the experimental results demonstrated that precision repairing machining can be achieved autonomously by using the system developed. Future work of this project will be focused on the online adaptive path generation and tracking to minimize line-to-line and layer-to-layer machining variation, and simultaneous force and path tracking.

References

[1] J. Oyekan, M. Farnsworth, W. Hutabarat, D. Miller, and A. Tiwari, “Applying a 6 dof robotic arm and digital twin to automate fan-blade reconditioning for aerospace maintenance, repair, and overhaul,” *Sensors*, vol. 20, no. 16, p. 4637, 2020.

[2] Y. K. Bandari, S. W. Williams, J. Ding, and F. Martina, “Additive manufacture of large structures: robotic or cnc systems?,” in *2014 International Solid Freeform Fabrication Symposium*, University of Texas at Austin, 2015.

[3] R. Chen, C. Zhou, and L.-l. Cheng, “Computer-vision-guided semi-autonomous concrete crack repair for infrastructure maintenance using a robotic arm,” *AI in Civil Engineering*, vol. 1, no. 1, pp. 1–16, 2022. Article number: 9.

[4] G. Du, K. Wang, S. Lian, and K. Zhao, “Vision-based robotic grasping from object localization, object pose estimation to grasp estimation for parallel grippers: a review,” *Artificial Intelligence Review*, vol. 54, no. 3, pp. 1677–1734, 2021.

[5] J. G. Pandya and N. P. Maniar, “Computer vision-guided human–robot collaboration for industry 4.0: A review,” *Recent Advances in Mechanical Infrastructure: Proceedings of ICRAM 2021*, pp. 147–155, 2022.

[6] N. Houshangi, “Control of a robotic manipulator to grasp a moving target using vision,” in *Proceedings., IEEE International Conference on Robotics and Automation*, pp. 604–609 vol.1, 1990.

[7] J. Kofman, X. Wu, T. Luu, and S. Verma, “Teleoperation of a robot manipulator using a vision-based human-robot interface,” *IEEE Transactions on Industrial Electronics*, vol. 52, no. 5, pp. 1206–1219, 2005.

[8] J. Kofman, X. Wu, T. Luu, and S. Verma, “Teleoperation of a robot manipulator using a vision-based human-robot interface,” *IEEE Transactions on Industrial Electronics*, vol. 52, no. 5, pp. 1206–1219, 2005.

[9] Z. Wang, R. Liu, T. Sparks, H. Liu, and F. Liou, “Stereo vision based hybrid manufacturing process for precision metal parts,” *Precision Engineering*, vol. 42, pp. 1–5, 2015.

[10] G. Flandin, F. Chaumette, and E. Marchand, “Eye-in-hand/eye-to-hand cooperation for visual servoing,” in *Proceedings 2000 ICRA. Millennium Conference. IEEE International Conference on Robotics and Automation. Symposia Proceedings (Cat. No. 00CH37065)*, vol. 3, pp. 2741–2746, IEEE, 2000.

[11] A. Kuss, M. Drust, and A. Verl, “Detection of workpiece shape deviations for tool path adaptation in robotic deburring systems,” *Procedia CIRP*, vol. 57, pp. 545–550, 2016.